

www.acsmaterialsletters.org

High Breakdown Current Density in Monolayer Nb₄C₃T_x MXene

Alexey Lipatov, Michael J. Loes, Nataliia S. Vorobeva, Saman Bagheri, Jehad Abourahma, Hanying Chen, Xia Hong, Yury Gogotsi, and Alexander Sinitskii*



Cite This: ACS Materials Lett. 2021, 3, 1088-1094



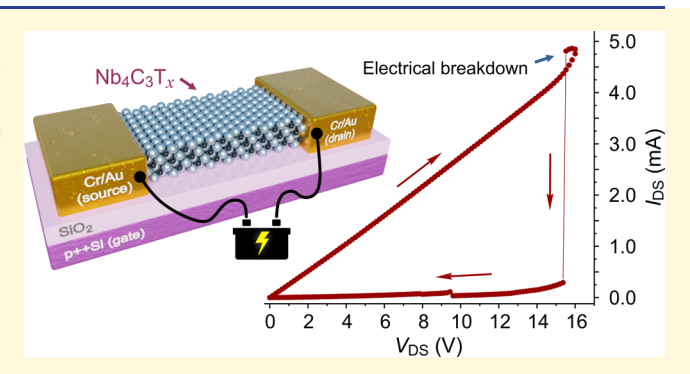
ACCESS I

III Metrics & More

Article Recommendations

Supporting Information

ABSTRACT: MXenes are an emerging family of transitionmetal carbides, nitrides, and carbonitrides that are promising for a variety of applications, including energy storage, gas sensors, and electromagnetic interference shielding. A recent report on a very high breakdown current density of $\sim 1.2 \times 10^8$ A cm⁻² in $Ti_3C_2T_x$ further extended the list of potential applications of MXenes to miniaturized on-chip interconnects. In this study, we investigated another promising member of the MXene family, Nb₄C₃T_x, and found that it also has a very high breakdown current density of ~1.1 × 10⁸ A cm⁻², which is comparable to that of Ti₃C₂T_x and other highly conductive twodimensional materials, such as graphene. The measurements



were performed on electronic devices based on individual monolayer flakes of Nb₄C₃T_x, which were tested at gradually increasing voltages until the electrical breakdown was observed. The morphology of Nb₄C₃T_x devices after the breakdown was studied by microscopic techniques. The high breakdown current densities of Ti₃C₂T_x and Nb₄C₃T_x suggest that other members of the large MXene family likely possess this property and could be employed in applications utilizing their high current-carrying capacity.

here is a growing interest in the synthesis, properties, and emerging applications of two-dimensional (2D) transition-metal carbides, nitrides, and carbonitrides, collectively known as MXenes. 1,2 These materials have a general formula $M_{n+1}X_nT_x$, where M is a transition metal, such as Ti, Nb, V, Ta, etc., X is carbon and/or nitrogen, Tx represents surface functional groups, and n = 1, 2, 3, or 4. MXene sheets are synthesized by selective etching of layers of an "A" element, such as Al or Si, from bulk crystals of layered MAX phases with a general formula $M_{n+1}AX_n$. Dozens of MAX phases have been reported,³ and in recent years, many of them have been subjected to the A-element etching, resulting in over 30 experimentally demonstrated MXene compositions, including $Ti_3C_2T_{x\nu}^{4}$ Nb₄C₃T_{x ν}5 Mo₄VC₄T_{x ν 6 and many}

Most experimental research so far has been focused on $Ti_3C_2T_{xy}^{-1}$ which is the first discovered MXene material.⁴ Ti₃C₂T_x has exceptional electronic and mechanical properties,^{7,8} which justify its promise for a large variety of applications ranging from energy storage 9,10 and photovoltaics¹¹ to electronic and photonic devices, ¹² gas sensors^{13,14} and electromagnetic interference shielding.¹⁵ A recent study demonstrated that Ti₃C₂T_x MXene also has a very high breakdown current density of $\sim 1.2 \times 10^8 \text{ A cm}^{-2,16}$ which

extends the list of potential applications of MXenes to miniaturized on-chip interconnects in integrated circuits. Considering that this is currently the only study of breakdown current density in MXenes, it is unclear whether this high reported value is unique for $Ti_3C_2T_x$ or if some other members of the large MXene family possess similar or even better characteristics.

In this study, we investigated the breakdown current density in monolayer Nb₄C₃T_r MXene (see the inset in Figure 1a). While $Ti_3C_2T_x$ had been the most popular MXene material so far, niobium carbides also received considerable attention as electrodes for Li ion batteries ^{17–19} and supercapacitors, ²⁰ catalyst supports, ²¹ free-radical scavengers, ²² phototherapeutic cancer treatments, ²³ and superconductors. ²⁴ The choice of $Nb_4C_3T_x$ for this study was further justified by the availability of the synthetic procedure enabling large (a few micrometers in size) well-exfoliated MXene flakes²⁵ that are necessary for

Received: June 1, 2021 Accepted: June 15, 2021 Published: June 28, 2021





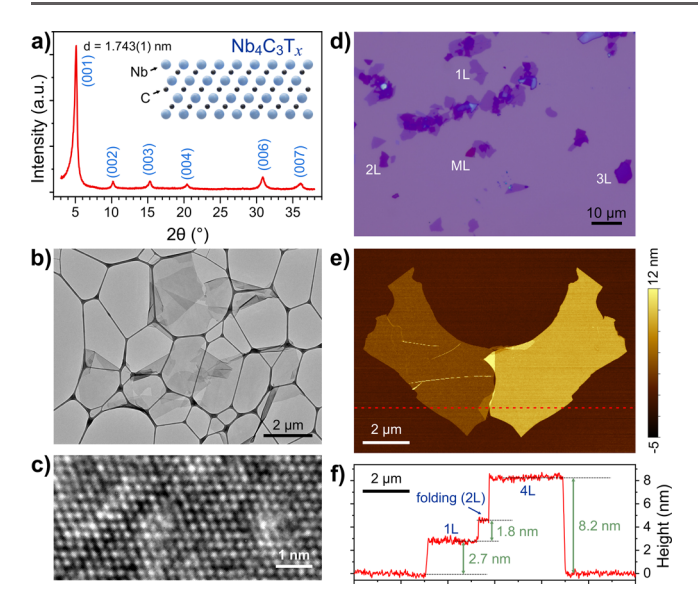


Figure 1. Characterization of the $\mathrm{Nb_4C_3T_x}$ flakes. (a) XRD pattern of a $\mathrm{Nb_4C_3T_x}$ film. The side view of a $\mathrm{Nb_4C_3T_x}$ MXene monolayer is shown in the inset; the blue spheres represent Nb; the black spheres represent C; the surface functional groups (T_x) are omitted. (b) TEM image of $\mathrm{Nb_4C_3T_x}$ flakes on a lacey carbon grid. (c) HRTEM image of a $\mathrm{Nb_4C_3T_x}$ flake. (d) Optical image of monolayer (1L), bilayer (2L), trilayer (3L), and multilayer (ML) $\mathrm{Nb_4C_3T_x}$ flakes on a $\mathrm{Si/SiO_2}$ substrate. (e) AFM image of a multilayer $\mathrm{Nb_4C_3T_x}$ flake next to a monolayer flake exfoliated from it. (f) Height profile measured along the red dashed line in the AFM image shown in panel (e).

nanofabrication of single-flake devices and their electrical measurements. 26

The synthesis of Nb₄C₃T_r MXene is described in our previous study²⁵ and summarized in the Supporting Information (SI). In brief, the synthetic procedure is based on the HF etching of Nb₄AlC₃ MAX phase⁵ and delamination of the resulting Nb₄C₃T_x using tetramethylammonium hydroxide (TMAOH). The procedure results in well-exfoliated Nb₄C₃T_x MXene material with a large fraction of fewmicrometer-sized flakes that could be conveniently used for device fabrication.²⁵ An aqueous solution of Nb₄C₃T_x MXene was drop-casted on a substrate and dried to form a thick film that was analyzed by X-ray diffraction (XRD). The measurement was performed using a Rigaku Smart Lab powder diffractometer with Ni-filtered Cu Klpha radiation. The XRD pattern shown in Figure 1a reveals a series of equidistantly spaced (00l) peaks ranging from (001) to (007), indicating a layered structure of stacked MXene flakes. The interplanar distance extracted from the XRD pattern of a Nb₄C₃T_x MXene film is ~1.743 nm, which is consistent with the previous measurements.²⁵ According to the results of X-ray photoelectron spectroscopy (XPS), the Nb₄C₃T_x MXene synthesized by the described HF etching route had a mixed O/F termination (see Figure S1 and its discussion in the SI).

The high quality of the $\mathrm{Nb_4C_3T_x}$ flakes used for the device fabrication was confirmed by transmission electron microscopy (TEM). Figure 1b shows uniform $\mathrm{Nb_4C_3T_x}$ flakes deposited on a lacey carbon TEM grid that are several micrometers in size. High-resolution transmission electron microscopy (HRTEM) of these flakes revealed the perfect hexagonal arrangement of the Nb atoms (Figure 1c). TEM was performed using a FEI

Tecnai Osiris scanning transmission electron microscope at an accelerating voltage of 200 kV.

A droplet of an aqueous suspension of Nb₄C₃T_r flakes was placed on a p-type silicon substrate covered with a 300-nmthick layer of SiO₂ and dried in air. Individual MXene flakes with different thicknesses can be identified by optical microscopy according to their optical contrast (Figure 1d). The thickness of the flakes was investigated by atomic force microscopy (AFM), which was performed using a Bruker Dimension Icon AFM system operated in the PeakForce tapping mode. Figure 1e shows an AFM image of a few-layer $Nb_4C_3T_x$ flake along with a monolayer flake of exactly the same shape. The shapes of these flakes suggest that they originated from the same Nb₄AlC₃ crystallite. The AFM height profile analysis shown in Figure 1f confirms our previous findings that the thickness of a monolayer Nb₄C₃T_x on Si/SiO₂ is \sim 2.7 nm, which is larger than its nominal thickness due to the presence of molecular adsorbates, such as water molecules, that are trapped between the substrate and the flake. 25 As we extensively discussed in our previous work, 25 Nb₄C₃T_x monolayers that are measured by AFM on top of other $Nb_4C_3T_x$ flakes have a smaller thickness of ~1.8 nm (see the folded region in Figures 1e and 1f), which is similar to the value obtained by the XRD analysis (1.74 nm). Given that, for a multilayer flake, the bottom layer lying directly on Si/SiO₂ has a thickness of 2.7 nm and each subsequent layer adds ~1.8 nm to the overall thickness, we conclude that the thicker flake in Figure 1e consists of four Nb₄C₃T_x monolayers (2.7 nm + $(3 \times 1.8 \text{ nm}) = 8.1 \text{ nm}).^{25}$

Several individual MXene flakes were identified by optical microscopy and used for patterning field-effect transistor (FET) devices by electron-beam lithography as described in our previous works. The scheme of a typical MXene device used in this study is presented in Figure 2a. It shows a Nb₄C₃T_x flake bridging Cr (5 nm)/Au (20 nm) source (S) and drain (D) electrodes on a Si/SiO₂ substrate; the conductive *p*-type Si layer served as the global back gate (G) electrode. Figure 2b shows a scanning electron microscopy (SEM) image of a representative device based on a bilayer Nb₄C₃T_x flake; the Cr/Au electrodes are highlighted in yellow for clarity. SEM was performed using a Zeiss Supra 40 field-emission SEM system at an accelerating voltage of 5 kV.

The room-temperature electrical measurements of $Nb_4C_3T_x$ devices were performed under vacuum in a Lake Shore TTPX probe station at the base pressure of $\sim 2 \times 10^{-6}$ Torr, using an Agilent 4155C semiconductor parameter analyzer. Prior to the measurements, the devices were kept under vacuum for at least 2 days to minimize the effect of surface adsorbates. ²⁷ The I_{DS} $V_{
m DS}$ dependences at three different gate voltages (-40, 0, and 40 V) for the device shown in Figure 2b are presented in Figure 2c. The linearity of the $I_{DS}-V_{DS}$ dependences is indicative of Ohmic contacts between the MXene channel and the electrodes, which is consistent with the previously reported results of four-terminal electrical measurements of devices based on Nb₄C₃T_x flakes with Cr/Au electrodes.²⁵ The superimposed I_{DS} – V_{DS} dependences measured at different V_G (Figure 2c) demonstrate the weak effect of gate voltage on the electrical conductivity of the device. The sheet resistances for the devices were calculated from the $I_{\rm DS}{-}V_{\rm DS}$ curves measured at $V_G = 0$ and the flake dimensions. The bilayer Nb₄C₃T_x device shown in Figure 2b has a sheet resistance of 3690 Ω \Box ⁻¹. MXene resistivity can then be calculated by dividing the sheet resistance by the flake thickness, which, for

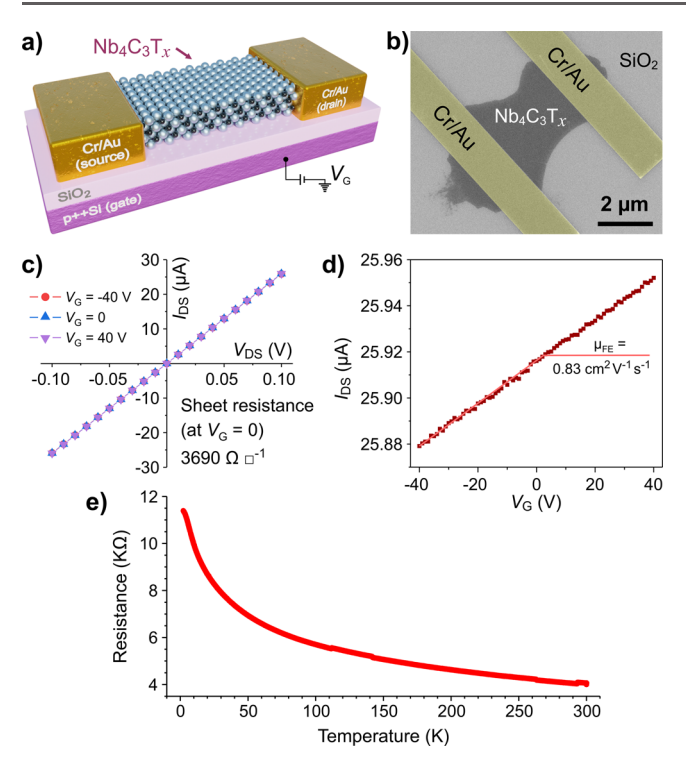


Figure 2. Electronic properties of Nb₄C₃T_x flakes. (a) Scheme of a two-terminal device based on an individual Nb₄C₃T_x flake. (b) SEM image of a representative device based on a bilayer Nb₄C₃T_x flake. The electrodes are colored in yellow for clarity. (c) $I_{\rm DS}-V_{\rm DS}$ dependences for the Nb₄C₃T_x device shown in panel (b) measured at the gate voltages of -40, 0, and 40 V. (d) $I_{\rm DS}-V_{\rm G}$ dependence for the same device measured at $V_{\rm DS}=0.1$ V. (e) Temperature dependence of resistance of the bilayer Nb₄C₃T_x FET shown in panel (b).

bilayer Nb₄C₃T_x, can be estimated to be ~2.52 nm.²⁵ The resulting resistivity for the MXene device shown in Figure 2b is 9.3 $\mu\Omega$ m and the corresponding conductivity is 1075 S cm⁻¹, both of which are in agreement with the previously published data for bilayer Nb₄C₃T_x flakes. Figure 2d shows the transfer characteristics for the same device measured at $V_{\rm DS}$ = 0.1 V in the $V_{\rm G}$ range from $-40~{\rm V}$ to $+40~{\rm V}$. The $I_{\rm DS}-V_{\rm G}$ dependence is linear and similar to our previous reports for MXene materials. 7,25 The positive slope of the $I_{\rm DS}{-}V_{\rm G}$ dependence is indicative of the *n*-type transport. Field-effect mobilities (μ_{FE}) were extracted from the transfer characteristics using the formula $\mu_{\rm FE} = C_{\rm d}^{-1} \times \partial \rho^{-1}/\partial V_{\rm G}$, where $C_{\rm d}$ is the capacitance of a 300-nm-thick SiO $_2$ dielectric layer and ρ is the resistivity of a $Nb_4C_3T_x$ device channel. For the bilayer $Nb_4C_3T_x$ device shown in Figure 2b, the calculated field-effect mobility is $\mu_{\rm FE}$ = 0.83 cm² V⁻¹ s⁻¹, which is larger than for typical monolayer $Nb_4C_3T_x$ flakes (~0.49 cm² V⁻¹ s⁻¹).²⁵

Temperature-dependent resistance measurements were performed in a Quantum Design physical property measurement system (PPMS). Figure 2e shows the temperature dependence of resistance for the same bilayer Nb₄C₃T_x MXene device (Figure 2b) in the temperature range from 2 K to 300 K. The resistance increases with decreasing temperature, which is in agreement with the previous reports on Nb₄C₃T_x films²⁸ and individual flakes, ²⁵ as well as several other MXenes. ^{29,30} Interestingly, a recent study demonstrated superconductivity above 4.2 K in Nb₂CT_x MXene with certain functional groups T, such as chlorine (Nb₂CCl₂ with a critical temperature (T_c)

of \sim 6.0 K), sulfur (Nb₂CS₂, $T_c \approx 6.4$ K), and selenium (Nb₂CSe₂, $T_c \approx 4.5$ K). ²⁴ In contrast, the HF-etched Nb₂CT_x MXene with a mixed O/F termination did not exhibit superconductivity in the same temperature range from 2 K to 300 K. ²⁴ The Nb₄C₃T_x MXene flakes that were also produced in this work by the HF etching route had a mixed O/F surface termination ^{20,25} (see the results of the XPS analysis in Figure S1 in the SI) and did not exhibit superconducting properties at temperatures above 2 K (Figure 2e), which is consistent with the results reported for the HF-etched Nb₂CT_x. ²⁴ However, these studies collectively suggest that superconductivity in Nb₄C₃T_x MXene may be achieved by a precise control of surface functionalities, which could be a promising topic for future studies.

Figure 3 shows a series of $I_{DS}-V_{DS}$ dependences that illustrate the current annealing and electrical breakdown in a representative monolayer Nb₄C₃T_x FET. The microscopic images of this device can be seen in Figure 4. The measurements were performed at $V_G = 0$, and each $I_{DS} - V_{DS}$ curve includes a forward $V_{\rm DS}$ scan from 0 to a certain value of $V_{\rm DS,max}$ and a reverse scan back to 0. Figure 3a shows that when the drain-source voltage was scanned from 0 to $V_{DS,max}$ ranging from 1 to 12 V and then scanned back to 0, the forward and reverse scans retraced each other, demonstrating the reversible operation of the device within this V_{DS} range. However, when the scan range was increased to 14 V, we started to observe irreversible changes to the device. This can be illustrated by Figure 3b, which shows six consecutive $I_{DS}-V_{DS}$ scans that were measured from 0 to $V_{\rm DS,max}$ = 14 V and then back to 0. Figure 3b demonstrates that starting with the first $I_{DS}-V_{DS}$ scan the reverse $V_{\rm DS}$ sweeps showed higher currents than the forward sweeps. The increased conductivity can be explained by the effect of current annealing, which is widely used to clean electronic devices based on other 2D materials, such as graphene, from adsorbed impurities by Joule heating and thus improve their transport characteristics. 31,3

In the first scan in Figure 3b (see the brown I_{DS} – V_{DS} curve), as the drain-source voltage approached $V_{\rm DS,max}$ = 14 V, the Joule heating became sufficient to improve the device conductivity, and as a result, in the reverse V_{DS} sweep the current was higher than in the forward sweep. Additional Joule heating could be performed by repeating the measurement. In the second forward V_{DS} sweep (see the dark orange curve in Figure 3b), the current coincides with the reverse sweep from the previous measurement, demonstrating that the conductivity improvement of the device is irreversible. Then, as the drain-source voltage approached $V_{\rm DS,max}$ = 14 V again, the Joule heating further improved the conductivity, and the reverse sweep again showed a higher current than in the forward sweep. Consecutive $I_{\rm DS} - V_{\rm DS}$ scans up to $V_{\rm DS,max}$ = 14 V further annealed the device, resulting in a noticeable conductivity improvement with each measurement, see Figure

Further annealing could be performed by increasing the drain—source voltage scan range up to $V_{\rm DS,max}=15~\rm V$ (Figure 3c) with the largest conductivity improvement observed in the first $I_{\rm DS}-V_{\rm DS}$ scan. However, when the $V_{\rm DS}$ scan range was increased up to $V_{\rm DS,max}=16~\rm V$, the generated Joule heat became sufficiently high to cause irreversible damage to the device and resulted in a dramatic loss of current in the reverse sweep (Figure 3d). For convenience, all $I_{\rm DS}-V_{\rm DS}$ scans from Figure 3a—d are plotted together in Figure 3e to demonstrate the gradual improvement of the device conductivity due to the

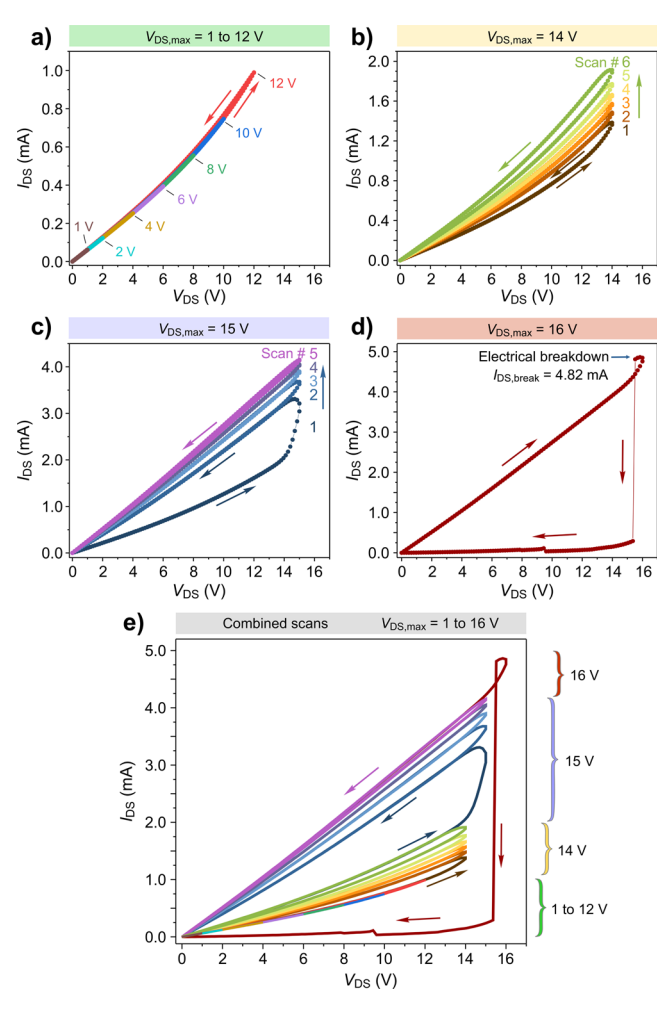


Figure 3. Stepwise current annealing and electrical breakdown of a monolayer $\mathrm{Nb_4C_3T_x}$ flake. (a) Seven consecutive $I_\mathrm{DS}{-}V_\mathrm{DS}$ measurements of the same flake, in which the voltage was scanned from 0 up to $V_\mathrm{DS,max}$ and then back to 0. In these measurements, $V_\mathrm{DS,max}$ was consecutively increased from 1 to 12 V. (b) Six consecutive $I_\mathrm{DS}{-}V_\mathrm{DS}$ measurements, in which the voltage was scanned from 0 up to $V_\mathrm{DS,max}$ = 14 V and then back to 0. (c) Five consecutive $I_\mathrm{DS}{-}V_\mathrm{DS}$ measurements, in which the voltage was scanned from 0 up to $V_\mathrm{DS,max}$ = 15 V and then back to 0. (d) Electrical breakdown of the monolayer $\mathrm{Nb_4C_3T_x}$ flake that occurred after the drain-source voltage was scanned from 0 to $V_\mathrm{DS,max}$ = 16 V after the measurements shown in panels (a)—(c). (e) All $I_\mathrm{DS}{-}V_\mathrm{DS}$ curves from panels (a)—(d) shown in the same plot for clarity.

Joule heating until the electrical breakdown after the sweep up to $V_{\rm DS,max}$ = 16 V.

The maximum current density of monolayer Nb₄C₃T_x was calculated using the formula $j_c = I_{\rm DS, max}/(wt)$, where $I_{\rm DS, max}$ is the maximum $I_{\rm DS}$ measured before the breakdown, w is the average channel width, and t is the thickness (1.26 nm for the monolayer Nb₄C₃T_x).²⁵ For the tested monolayer Nb₄C₃T_x devices, the average j_c is $1.05 \pm 0.11 \times 10^8$ A cm⁻². To put this value in context, we can compare this result with the breakdown current densities of other important electronic materials. The j_c value for Nb₄C₃T_x is at least two orders of magnitude larger than the breakdown current density of copper, which is the most common interconnect material, $^{33-35}$ demonstrating the potential promise of Nb₄C₃T_x MXene for interconnect applications. Compared to other 2D materials,

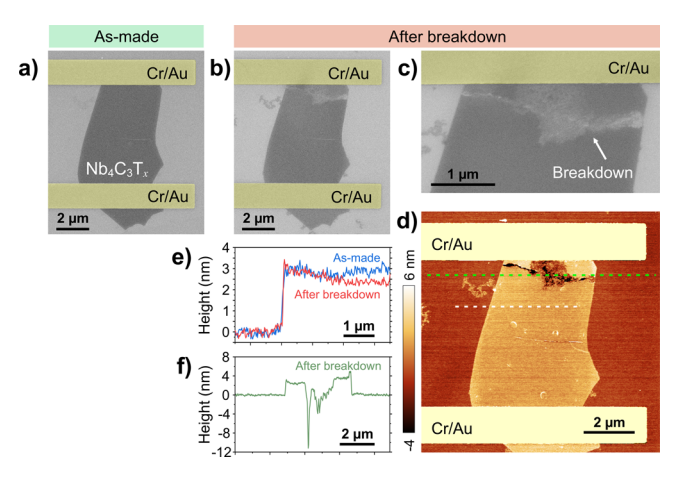


Figure 4. Effect of electrical breakdown on the morphology of a monolayer $\mathrm{Nb_4C_3T_x}$ flake. (a) SEM image of a device based on a monolayer $\mathrm{Nb_4C_3T_x}$ flake before the electrical testing. (b, c) SEM images of the same $\mathrm{Nb_4C_3T_x}$ device after the electrical breakdown. Panel (c) shows the close-up view of the breakdown area. The Cr/Au contacts in panels (a)—(c) are highlighted in yellow for clarity. (d) AFM image of the same $\mathrm{Nb_4C_3T_x}$ device after the electrical breakdown. The Cr/Au contacts are out of the range of the height scale bar. (e) AFM height profiles measured across the $\mathrm{Nb_4C_3T_x}$ flake along the white dashed line in panel (d) before and after the electrical breakdown. (f) AFM height profile of the damaged area of the flake measured along the green dashed line in panel (d).

the breakdown current density of monolayer Nb₄C₃T_x is much higher than for typical transition metal dichalcogenides, such as MoS₂ and WTe₂, 36,37 and is comparable to the materials with the highest j_c values on the order of 10^8 A cm $^{-2}$, including graphene, $^{33-35}$ ZrTe₃, 38 TaSe₃, $^{39-41}$ and single-walled carbon nanotubes. 42 Interestingly, the breakdown current density of Nb₄C₃T_x is very close to that of Ti₃C₂T_x MXene, which was recently reported to be $\sim 1.2 \times 10^8$ A cm $^{-2}$. 16 This observation suggests that a high breakdown current density is not an exclusive characteristic of Ti₃C₂T_x, but many other members of the large family of MXenes likely possess this property and could be employed in applications utilizing their high current-carrying capacity.

Figure 4 demonstrates the structural damage to monolayer $\mathrm{Nb_4C_3T_x}$ due to the electrical breakdown. Figure 4a shows SEM image of a representative monolayer $\mathrm{Nb_4C_3T_x}$ FET before the electrical characterization; the results of electrical measurements of this device are shown in Figure 3. After the $I_\mathrm{DS}-V_\mathrm{DS}$ scan up to $V_\mathrm{DS,max}=16$ V, which resulted in the electrical breakdown (Figure 3d), this FET was imaged by SEM again, revealing a crack across the $\mathrm{Nb_4C_3T_x}$ device channel, as shown in Figures 4b and 4c. Similar appearance of devices upon electrical breakdown was previously observed for $\mathrm{Ti_3C_2T_x}$ MXene, 16 as well as other materials, such as amorphous carbon 43 and graphene. 34

The changes to the $\mathrm{Nb_4C_3T_x}$ device morphology due to the electrical breakdown were also investigated by AFM (Figure 4d). Figure 4e shows two AFM height profiles that were measured across the same area of the $\mathrm{Nb_4C_3T_x}$ flake (see the white dashed line in Figure 4d) before and after the electrical breakdown. While the nominal thickness of monolayer $\mathrm{Nb_4C_3T_x}$ can be estimated to be ~ 1.26 nm, $^{2.5}$ the measured AFM height of the as-prepared flake was ~ 2.9 nm (Figure 4e), which could be explained by the presence of molecular adsorbates, such as water molecules, trapped under the flake.

When the same area of the device channel was measured again following the electrical breakdown, the flake thickness decreased down to 2.3 nm (Figure 4e), which can be explained by the partial removal of the adsorbates due to the Joule heating, as discussed above. However, the most significant change in the Nb₄C₃T_x flake height was observed in the breakdown area. The height profile measured across the crack formed in the Nb₄C₃T_x flake due to the electrical breakdown shows an indentation that is several nanometers deep, thus extending into the SiO₂ dielectric layer (see Figure 4f). The observed damage to SiO₂, which has a melting point of about 1700 °C, is consistent with the very high current density and the associated Joule heating that a monolayer Nb₄C₃T_x can withstand before the breakdown.

While we have primarily discussed the results of electrical breakdown experiments on monolayer Nb₄C₃T_x flakes, we also performed such experiments on bilayer flakes (see Figures S2 and S3 and their discussion in the SI). Some of the flakes exhibited interesting morphology after the breakdown, where large pieces of the flakes were apparently torn and blasted off the substrate during the electrical measurements (see Figures S2 and S3). This behavior could be attributed to the Joule heating of the intercalated molecules, primarily water, between the MXene layers, which resulted in the rapid expansion of the interlayer region, causing the flake damage. The main conclusion from these observations is that the interfacial phenomena should be seriously considered if Nb₄C₃T_x MXene will be scaled from individual monolayers with excellent current-carrying properties to large-scale interconnects with multiple interfaces between the flakes.

In summary, we found that Nb₄C₃T_x MXene has a very high breakdown current density of $\sim \! 1.1 \times 10^8$ A cm $^{-2}$, which is comparable to the best 2D materials, including graphene and Ti₃C₂T_x MXene. The latter comparison suggests that a high breakdown current density is not an exclusive characteristic of Ti₃C₂T_x. Many other members of the large MXene family 1,2 likely possess this property and could be employed in applications that take advantage of their high current-carrying capacity.

ASSOCIATED CONTENT

Solution Supporting Information

The Supporting Information is available free of charge at https://pubs.acs.org/doi/10.1021/acsmaterialslett.1c00324.

Synthesis of $Nb_4C_3T_x$ MXene; XPS characterization of $Nb_4C_3T_x$ MXene; electrical breakdown data for bilayer $Nb_4C_3T_x$ MXene flakes (PDF) (PDF)

AUTHOR INFORMATION

Corresponding Author

Alexander Sinitskii — Department of Chemistry and Nebraska Center for Materials and Nanoscience, University of Nebraska-Lincoln, Lincoln, Nebraska 68588, United States; orcid.org/0000-0002-8688-3451; Email: sinitskii@unl.edu

Authors

Alexey Lipatov — Department of Chemistry, University of Nebraska-Lincoln, Lincoln, Nebraska 68588, United States; orcid.org/0000-0001-5043-1616

Michael J. Loes – Department of Chemistry, University of Nebraska-Lincoln, Lincoln, Nebraska 68588, United States Nataliia S. Vorobeva — Department of Chemistry, University of Nebraska-Lincoln, Lincoln, Nebraska 68588, United States Saman Bagheri — Department of Chemistry, University of Nebraska-Lincoln, Lincoln, Nebraska 68588, United States

Jehad Abourahma – Department of Chemistry, University of Nebraska-Lincoln, Lincoln, Nebraska 68588, United States

Hanying Chen – Department of Physics and Astronomy, University of Nebraska-Lincoln, Lincoln, Nebraska 68588, United States

Xia Hong — Department of Physics and Astronomy, University of Nebraska-Lincoln, Lincoln, Nebraska 68588, United States; Nebraska Center for Materials and Nanoscience, University of Nebraska-Lincoln, Lincoln, Nebraska 68588, United States; Occid.org/0000-0002-7873-5774

Yury Gogotsi — A.J. Drexel Nanomaterials Institute and Department of Materials Science & Engineering, Drexel University, Philadelphia, Pennsylvania 19104, United States; orcid.org/0000-0001-9423-4032

Complete contact information is available at: https://pubs.acs.org/10.1021/acsmaterialslett.1c00324

Author Contributions

The manuscript was written through contributions of all authors. All authors have given approval to the final version of the manuscript.

Notes

The authors declare no competing financial interest.

ACKNOWLEDGMENTS

This work was supported by the Nebraska Public Power District through the Nebraska Center for Energy Sciences Research (NCESR) and the National Science Foundation (NSF) through the Nebraska Materials Research Science and Engineering Center (MRSEC) (No. DMR-1420645). The materials characterization was performed in part in the Nebraska Nanoscale Facility: National Nanotechnology Coordinated Infrastructure and the Nebraska Center for Materials and Nanoscience, which are supported by the NSF (No. ECCS-2025298) and the Nebraska Research Initiative. Development of MXenes at Drexel University was supported by the NSF (Grant No. DMR- 2041050).

REFERENCES

- (1) Gogotsi, Y.; Anasori, B. The Rise of MXenes. ACS Nano 2019, 13, 8491-8494.
- (2) Fu, Z.; Wang, N.; Legut, D.; Si, C.; Zhang, Q.; Du, S.; Germann, T. C.; Francisco, J. S.; Zhang, R. Rational Design of Flexible Two-Dimensional MXenes with Multiple Functionalities. *Chem. Rev.* **2019**, *119*, 11980–12031.
- (3) Barsoum, M. W. The $M_{N+1}A_XN$ phases: A new class of solids: Thermodynamically stable nanolaminates. *Prog. Solid State Chem.* **2000**, 28, 201–281.
- (4) Naguib, M.; Kurtoglu, M.; Presser, V.; Lu, J.; Niu, J.; Heon, M.; Hultman, L.; Gogotsi, Y.; Barsoum, M. W. Two-dimensional nanocrystals produced by exfoliation of Ti₃AlC₂. *Adv. Mater.* **2011**, 23, 4248–4253.
- (5) Ghidiu, M.; Naguib, M.; Shi, C.; Mashtalir, O.; Pan, L. M.; Zhang, B.; Yang, J.; Gogotsi, Y.; Billinge, S. J. L.; Barsoum, M. W. Synthesis and characterization of two-dimensional Nb_4C_3 (MXene). *Chem. Commun.* **2014**, *50*, 9517–9520.
- (6) Deysher, G.; Shuck, C. E.; Hantanasirisakul, K.; Frey, N. C.; Foucher, A. C.; Maleski, K.; Sarycheva, A.; Shenoy, V. B.; Stach, E. A.; Anasori, B.; Gogotsi, Y. Synthesis of Mo₄VAlC₄ MAX Phase and Two-

- Dimensional Mo₄VC₄ MXene with Five Atomic Layers of Transition Metals. ACS Nano 2020, 14, 204–217.
- (7) Lipatov, A.; Alhabeb, M.; Lukatskaya, M. R.; Boson, A.; Gogotsi, Y.; Sinitskii, A. Effect of synthesis on quality, electronic properties and environmental stability of individual monolayer ${\rm Ti_3}C_2$ MXene flakes. *Adv. Electron. Mater.* **2016**, *2*, 1600255.
- (8) Lipatov, A.; Lu, H.; Alhabeb, M.; Anasori, B.; Gruverman, A.; Gogotsi, Y.; Sinitskii, A. Elastic Properties of 2D Ti₃C₂T_x MXene Monolayers and Bilayers. *Sci. Adv.* **2018**, *4*, No. eaat0491.
- (9) Anasori, B.; Lukatskaya, M. R.; Gogotsi, Y. 2D metal carbides and nitrides (MXenes) for energy storage. *Nat. Rev. Mater.* **2017**, 2, 16098.
- (10) Pomerantseva, E.; Gogotsi, Y. Two-dimensional heterostructures for energy storage. *Nature Energy* **2017**, *2*, 17089.
- (11) Agresti, A.; Pazniak, A.; Pescetelli, S.; Di Vito, A.; Rossi, D.; Pecchia, A.; Auf der Maur, M.; Liedl, A.; Larciprete, R.; Kuznetsov, D. V.; Saranin, D.; Di Carlo, A. Titanium-carbide MXenes for work function and interface engineering in perovskite solar cells. *Nat. Mater.* **2019**, *18*, 1228–1234.
- (12) Kim, H.; Alshareef, H. N. MXetronics: MXene-Enabled Electronic and Photonic Devices. *ACS Materials Letters* **2020**, *2*, 55–70.
- (13) Kim, S. J.; Koh, H.-J.; Ren, C. E.; Kwon, O.; Maleski, K.; Cho, S.-Y.; Anasori, B.; Kim, C.-K.; Choi, Y.-K.; Kim, J.; Gogotsi, Y.; Jung, H.-T. Metallic ${\rm Ti}_3{\rm C}_2{\rm T}_x$ MXene Gas Sensors with Ultrahigh Signal-to-Noise Ratio. *ACS Nano* **2018**, *12*, 986–993.
- (14) Pazniak, H.; Plugin, I. A.; Loes, M. J.; Inerbaev, T. M.; Burmistrov, I. N.; Gorshenkov, M.; Polcak, J.; Varezhnikov, A. S.; Sommer, M.; Kuznetsov, D. V.; Bruns, M.; Fedorov, F. S.; Vorobeva, N. S.; Sinitskii, A.; Sysoev, V. V. Partially Oxidized Ti₃C₂T_x MXenes for Fast and Selective Detection of Organic Vapors at Part-per-Million Concentrations. *ACS Appl. Nano Mater.* **2020**, *3*, 3195–3204.
- (15) Shahzad, F.; Alhabeb, M.; Hatter, C. B.; Anasori, B.; Man Hong, S.; Koo, C. M.; Gogotsi, Y. Electromagnetic interference shielding with 2D transition metal carbides (MXenes). *Science* **2016**, 353, 1137–1140.
- (16) Lipatov, A.; Goad, A.; Loes, M. J.; Vorobeva, N. S.; Abourahma, J.; Gogotsi, Y.; Sinitskii, A. High electrical conductivity and breakdown current density of individual monolayer Ti₃C₂T_x MXene flakes. *Matter* **2021**, *4*, 1413–1427.
- (17) Naguib, M.; Halim, J.; Lu, J.; Cook, K. M.; Hultman, L.; Gogotsi, Y.; Barsoum, M. W. New Two-Dimensional Niobium and Vanadium Carbides as Promising Materials for Li-Ion Batteries. *J. Am. Chem. Soc.* **2013**, *135*, 15966–15969.
- (18) Mashtalir, O.; Lukatskaya, M. R.; Zhao, M.-Q.; Barsoum, M. W.; Gogotsi, Y. Amine-Assisted Delamination of Nb₂C MXene for Li-Ion Energy Storage Devices. *Adv. Mater.* **2015**, *27*, 3501–3506.
- (19) Zhao, S.; Meng, X.; Zhu, K.; Du, F.; Chen, G.; Wei, Y.; Gogotsi, Y.; Gao, Y. Li-ion uptake and increase in interlayer spacing of Nb₄C₃ MXene. *Energy Storage Materials* **2017**, *8*, 42–48.
- (20) Zhao, S.; Chen, C.; Zhao, X.; Chu, X.; Du, F.; Chen, G.; Gogotsi, Y.; Gao, Y.; Dall'Agnese, Y. Flexible Nb₄C₃T_x Film with Large Interlayer Spacing for High-Performance Supercapacitors. *Adv. Funct. Mater.* **2020**, *30*, 2000815.
- (21) Li, Z.; Cui, Y.; Wu, Z.; Milligan, C.; Zhou, L.; Mitchell, G.; Xu, B.; Shi, E.; Miller, J. T.; Ribeiro, F. H.; Wu, Y. Reactive metal-support interactions at moderate temperature in two-dimensional niobium-carbide-supported platinum catalysts. *Nature Catalysis* **2018**, *1*, 349–355.
- (22) Ren, X.; Huo, M.; Wang, M.; Lin, H.; Zhang, X.; Yin, J.; Chen, Y.; Chen, H. Highly Catalytic Niobium Carbide (MXene) Promotes Hematopoietic Recovery after Radiation by Free Radical Scavenging. *ACS Nano* **2019**, *13*, 6438–6454.
- (23) Lin, H.; Gao, S.; Dai, C.; Chen, Y.; Shi, J. A Two-Dimensional Biodegradable Niobium Carbide (MXene) for Photothermal Tumor Eradication in NIR-I and NIR-II Biowindows. *J. Am. Chem. Soc.* **2017**, 139, 16235–16247.
- (24) Kamysbayev, V.; Filatov, A. S.; Hu, H.; Rui, X.; Lagunas, F.; Wang, D.; Klie, R. F.; Talapin, D. V. Covalent surface modifications

- and superconductivity of two-dimensional metal carbide MXenes. *Science* **2020**, *369*, 979–983.
- (25) Lipatov, A.; Alhabeb, M.; Lu, H.; Zhao, S.; Loes, M. J.; Vorobeva, N. S.; Dall'Agnese, Y.; Gao, Y.; Gruverman, A.; Gogotsi, Y.; Sinitskii, A. Electrical and Elastic Properties of Individual Single-Layer Nb₄C₃T_x MXene Flakes. *Advanced Electronic Materials* **2020**, *6*, 1901382.
- (26) Lipatov, A.; Sinitskii, A., Electronic and Mechanical Properties of MXenes Derived from Single-Flake Measurements. In 2D Metal Carbides and Nitrides (MXenes): Structure, Properties and Applications; Anasori, B., Gogotsi, Y., Eds.; Springer International Publishing: Cham, Switzerland, 2019; pp 301–325.
- (27) Sinitskii, A.; Dimiev, A.; Kosynkin, D. V.; Tour, J. M. Graphene Nanoribbon Devices Produced by Oxidative Unzipping of Carbon Nanotubes. *ACS Nano* **2010**, *4*, 5405–5413.
- (28) Halim, J.; Palisaitis, J.; Lu, J.; Thörnberg, J.; Moon, E. J.; Precner, M.; Eklund, P.; Persson, P. O. Å.; Barsoum, M. W.; Rosen, J. Synthesis of Two-Dimensional Nb_{1,33}C (MXene) with Randomly Distributed Vacancies by Etching of the Quaternary Solid Solution (Nb_{2/3}Sc_{1/3})₂AlC MAX Phase. ACS Appl. Nano Mater. **2018**, 1, 2455–2460.
- (29) Hantanasirisakul, K.; Alhabeb, M.; Lipatov, A.; Maleski, K.; Anasori, B.; Salles, P.; Ieosakulrat, C.; Pakawatpanurut, P.; Sinitskii, A.; May, S. J.; Gogotsi, Y. Effects of Synthesis and Processing on Optoelectronic Properties of Titanium Carbonitride MXene. *Chem. Mater.* **2019**, *31*, 2941–2951.
- (30) Anasori, B.; Shi, C.; Moon, E. J.; Xie, Y.; Voigt, C. A.; Kent, P. R. C.; May, S. J.; Billinge, S. J. L.; Barsoum, M. W.; Gogotsi, Y. Control of electronic properties of 2D carbides (MXenes) by manipulating their transition metal layers. *Nanoscale Horizons* **2016**, 1, 227–234.
- (31) Moser, J.; Barreiro, A.; Bachtold, A. Current-induced cleaning of graphene. *Appl. Phys. Lett.* **2007**, *91*, 163513.
- (32) Bolotin, K. I.; Sikes, K. J.; Jiang, Z.; Klima, M.; Fudenberg, G.; Hone, J.; Kim, P.; Stormer, H. L. Ultrahigh electron mobility in suspended graphene. *Solid State Commun.* **2008**, *146*, 351–355.
- (33) Murali, R.; Yang, Y.; Brenner, K.; Beck, T.; Meindl, J. D. Breakdown current density of graphene nanoribbons. *Appl. Phys. Lett.* **2009**, *94*, 243114.
- (34) Prins, F.; Barreiro, A.; Ruitenberg, J. W.; Seldenthuis, J. S.; Aliaga-Alcalde, N.; Vandersypen, L. M. K.; Van Der Zant, H. S. J. Room-Temperature Gating of Molecular Junctions Using Few-Layer Graphene Nanogap Electrodes. *Nano Lett.* **2011**, *11*, 4607–4611.
- (35) Yu, J.; Liu, G.; Sumant, A. V.; Goyal, V.; Balandin, A. A. Graphene-on-Diamond Devices with Increased Current-Carrying Capacity: Carbon sp²-on-sp³ Technology. *Nano Lett.* **2012**, *12*, 1603–1608.
- (36) Lembke, D.; Kis, A. Breakdown of High-Performance Monolayer MoS₂ Transistors. ACS Nano **2012**, 6, 10070–10075.
- (37) Mleczko, M. J.; Xu, R. L.; Okabe, K.; Kuo, H.-H.; Fisher, I. R.; Wong, H. S. P.; Nishi, Y.; Pop, E. High Current Density and Low Thermal Conductivity of Atomically Thin Semimetallic WTe₂. ACS Nano **2016**, 10, 7507–7514.
- (38) Geremew, A.; Bloodgood, M. A.; Aytan, E.; Woo, B. W. K.; Corber, S. R.; Liu, G.; Bozhilov, K.; Salguero, T. T.; Rumyantsev, S.; Rao, M. P.; Balandin, A. A. Current Carrying Capacity of Quasi-1D ZrTe₃ Van Der Waals Nanoribbons. *IEEE Electron Device Lett.* **2018**, 39, 735–738.
- (39) Empante, T. A.; Martinez, A.; Wurch, M.; Zhu, Y.; Geremew, A. K.; Yamaguchi, K.; Isarraraz, M.; Rumyantsev, S.; Reed, E. J.; Balandin, A. A.; Bartels, L. Low Resistivity and High Breakdown Current Density of 10 nm Diameter van der Waals TaSe₃ Nanowires by Chemical Vapor Deposition. *Nano Lett.* **2019**, *19*, 4355–4361.
- (40) Stolyarov, M. A.; Liu, G.; Bloodgood, M. A.; Aytan, E.; Jiang, C.; Samnakay, R.; Salguero, T. T.; Nika, D. L.; Rumyantsev, S. L.; Shur, M. S.; Bozhilov, K. N.; Balandin, A. A. Breakdown current density in *h*-BN-capped quasi-1D TaSe₃ metallic nanowires: prospects of interconnect applications. *Nanoscale* **2016**, *8*, 15774–15782.

(41) Liu, G.; Rumyantsev, S.; Bloodgood, M. A.; Salguero, T. T.; Shur, M.; Balandin, A. A. Low-Frequency Electronic Noise in Quasi-1D TaSe₃ van der Waals Nanowires. *Nano Lett.* **2017**, *17*, *377*—383. (42) Javey, A.; Qi, P.; Wang, Q.; Dai, H. Ten- to 50-nm-long quasi-ballistic carbon nanotube devices obtained without complex lithography. *Proc. Natl. Acad. Sci. U. S. A.* **2004**, *101*, 13408—13410. (43) Sinitskii, A.; Tour, J. M. Lithographic Graphitic Memories. *ACS Nano* **2009**, *3*, 2760—2766.